Supercell Models of Brønsted and Lewis Sites in Zeolites

56

Sichi Li and William F. Schneider

Contents

Abstract

Zeolites are three-dimensional, crystalline silicate-based materials of interest for catalysis and separations. Computational models of zeolites must capture their three-dimensional structure, the intrinsic microscopic heterogeneity introduced by heteroatom substitutions that underlie their interesting chemical behavior, and the dynamic nature of reactive sites within the pores of molecular dimensions. Here we describe the use of supercell density functional theory (DFT) models for tackling these problems, focusing primarily on Brønsted acidic and Cu-exchanged chabazite (CHA) zeolites and their chemistry related to the catalytic

S. Li · W. F. Schneider (✉)
Department of Chemical and Biomolecular Engineering, University of Notre Dame, Notre Dame, IN, USA
e-mail: sli12@nd.edu; wschneider@nd.edu

W. Andreoni, S. Yip (eds.), *Handbook of Materials Modeling*,
https://doi.org/10.1007/978-3-319-44680-6_4

chemistry of nitrogen oxides (NO_x). We describe considerations important in model construction, applications of *ab initio* molecular dynamics to structure annealing and accurate computations of reaction and activation free energies, first-principles thermodynamics approaches for predicting site compositions at realistic conditions, and approaches for incorporating heteroatom distributions into material models.

1 Introduction

Zeolites are a general class of crystalline silicate-based materials (Auerbach et al. 2003). The presence of micropores and voids of fixed, molecular dimension and the ability to tailor through chemical functionalization make them broadly useful as catalysts ranging from fluid catalytic cracking (Corma 1989) to hydrocarbon oligomerization (Nicholas 2017) to selective catalytic reduction (SCR) of NO_x with NH_3 (Paolucci et al. 2016a). The primary building unit of a zeolite is an SiO_4 tetrahedron (or T-site), which can be linked together at the corners to create a variety of secondary building units, including rings and cages of various sizes, that are further organized into distinct three-dimensional, periodic structures. The topology of a zeolite determines the sizes and dimensionalities of pores that permit molecular access into the interior of the zeolite as well as the sizes and interconnectivities of any cages. The identity of a zeolite is further nuanced by its chemical composition, including the types, concentrations, and locations of any framework or extra-framework heteroatoms. Depending on the synthesis method and treatment history, heteroatoms can be distributed in different ways, e.g., substituting framework Si (Lopez et al. 1993; Matsubayashi et al. 1996), cationically charge-compensating anionic framework blocks (Sherry 1966; Colella 1996), or even forming aggregated metal clusters or metal oxides inside the zeolite cages (Melson et al. 1983). Substitution of framework Si by Al is the most common chemical modification of a zeolite. Due to the 3+ oxidation state of Al, each substitution of a 4+ Si introduces a negatively charged site that can in principle host an extra-framework cation, e.g., a proton, alkali metal, or transition metals. These substituents introduce distinct chemical functionality into the zeolite, such as Lewis acidity or basicity, Brønsted acidity, and/or redox activity, all relevant to catalysis by enhancement of adsorption and/or bond activation of reactant(s) and intermediate(s). How to accurately model the electronic properties of different cations in zeolites from first-principles has been a popular topic in the computational catalysis community for many years (Sauer et al. 1980; Trout et al. 1996; Schneider et al. 1998; Gonzales et al. 1998; Sierka and Sauer 2001; Tuma and Sauer 2006; Paolucci et al. 2016b).

The two common approaches to represent a zeolite within an atomistic simulation are cluster and supercell models. The basic idea of cluster model is to excise the relevant portion of the zeolite framework (a cluster) out of the three-dimensional structure. These cluster representations are amenable to treatment with standard local-basis-set quantum mechanical (QM) methods (Kramer et al. 1991). To recover the effect of zeolite confinement on chemistry, larger models are often created in

which the central cluster containing the chemically relevant active site is treated with QM and a surrounding silicate cage is treated at some lower level of theory (Sherwood et al. 1997; Sierka and Sauer 2005). Such hybrid quantum mechanics-molecular mechanics (QM/MM) methods potentially offer computational efficiency combined with the accuracy of general QM methods. These models take some care to construct and are not well suited to problems in which the site of interest is not well known or well localized. A more natural approach to modeling a zeolite is to apply a supercell approach in which periodic boundary conditions (PBC) are used to naturally recover the dimensionality of a zeolite structure (Rozanska et al. 2003; Hafner 2008). The periodic nature of a supercell model is well suited to plane-wave density functional theory (DFT) treatment and also enables ready implementation of ab initio molecular dynamics (AIMD) simulations to study dynamics behavior of the material (Hass et al. 1998). In this contribution, several common static DFT and state-of-the-art dynamics approaches as well as systematic strategies to model exchanged cation properties in Al-substituted zeolites using supercell model are described. Emphases are placed on methodologies used to probe Brønsted acidity, reactivity of exchange protons, Lewis acidity, siting preference, and redox thermodynamics of exchanged metal cations.

2 Brønsted Acid Site Modeling

A proton is the simplest form of an exchanged cation present in a zeolite, typically residing at one of the tetrahedrally coordinated oxygen atoms around the Al center. Exchanged protons contribute to the Brønsted acidity of a zeolite, which is vital to a broad spectrum of acid-catalyzed reactions. The Brønsted acid strength can influence catalytic activity and is determined by the local environment and accessibility of the protons, as determined by framework topology, type of T-site, different framework oxygen adjacent to each T-site, etc. For example, the MFI zeolite framework contains 12 symmetry-distinct T-sites with 4 first-shell oxygen atom for each, yielding in principle 48 different types of Brønsted acid sites in total, which can all be captured by an orthorhombic supercell as shown in Fig. 1. Experimentally observed Brønsted acid properties are generally an ensemble-average among all possible sites. In order to build the structure-property relationship of Brønsted acids, it is more straightforward and unambiguous to simulate each site explicitly through first-principles modeling than deconvolution from experimental observations.

2.1 Deprotonation Energy

One fundamental electronic property of a Brønsted acid site is the interaction strength between the proton and the anionic framework block, which can be quantified by a deprotonation energy (DPE), defined as the energy to move a proton from a Brønsted acid site into a noninteracting environment. DPE is therefore a

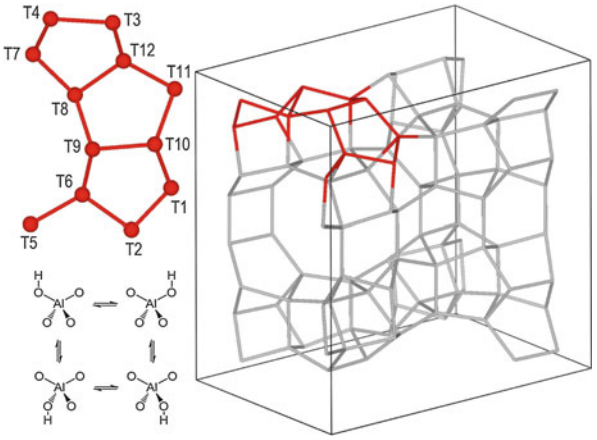

Fig. 1 Orthorhombic MFI zeolite supercell with 12 structural-unique T-sites highlighted and indexed. Four possible Brønsted acid site structures associated with single T-site Al are illustrated. (Adapted from Hernandez-Tamargo et al. 2016)

direct descriptor of the acid strength of a Brønsted acid site. Here we adopt the common "Z" shorthand as a symbol for an Al-substituted tetrahedral site in a zeolite. DPE formally corresponds to the energy of the reaction

$$\mathrm{DPE} = E_{\mathrm{Z}^-} + E_{\mathrm{H}^+} - E_{\mathrm{ZH}} \tag{1}$$

where E_{Z^-}, E_{H^+}, and E_{ZH} are DFT-computed 0-K energies of the anionic zeolite framework after deprotonation, an isolated proton, and neutral zeolite framework with a Brønsted acid site, respectively. Comprehensive studies of DPE for a variety of zeolite frameworks have been reported by several authors (Jones and Iglesia 2015; Rybicki and Sauer 2015). It is worthy to note that within the PBC, supercell model, calculations on the charged anionic zeolite framework or gaseous proton suffer from electrostatic interactions between the periodic images that can lead to erroneous DFT energies without appropriate corrections. One should use caution while trying to compare Brønsted acid strength using PBC DFT-computed DPE values across zeolite framework topologies because the degree of periodic image interaction artifact depends on supercell size as well as void fraction of the cell (Jones and Iglesia 2015).

2.2 Probe Molecule Binding

An alternative approach to quantify Brønsted acid strength is to calculate binding strength of a basic probe molecule, commonly NH_3, to the acid site. It is noteworthy that, unlike deprotonation energy, probe molecule binding strength is not determined only by the acid strength but also the local environment of the acid site through van der Waals interaction and/or hydrogen bonding with the zeolite framework (Jones and Iglesia 2015). Consequently, the net binding strength is the summation

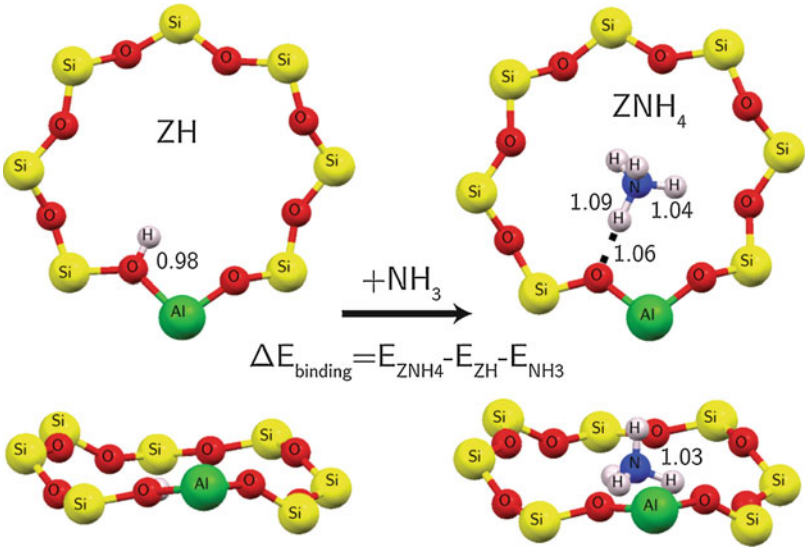

Fig. 2 DFT-optimized structures of ZH and ZNH_4. Only eight-membered rings and adsorbates are illustrated. Distances are given in Å. Equation of NH_3 binding energy calculation is inserted (Li et al. 2017)

of acid-base interaction and other weak interactions that are sensitive to framework pore and ring structure surrounding the Al substituted T-site.

Figure 2 presents an example in which NH_3 is used to probe the Brønsted acid strength of chabazite (CHA) zeolite (Li et al. 2017). The CHA lattice contains only one type of symmetry-distinct T-site, and the entire structure can be representing within a 12-T-site supercell. In a first step, DFT calculations were performed to search for the lowest energy structures of each species, including searches over the four distinct first-shell oxygen atoms adjacent to a substituted Al where a proton can locate. To identify the most favorable proton position, DFT geometry optimization calculations were performed for ZH structures with various proton positions. When NH_3 is placed close to a Brønsted acid, the location of energy minima becomes more challenging, as NH_3 extracts the H^+ from the framework to create an NH_4^+ that exhibits multiple local minima that are close in energy. In such situations, AIMD simulations at elevated temperatures are useful for sampling the potential energy surface. Low energy structures visited in the AIMD trajectory can be further relaxed to their ground states to collect local and, ideally, the global minimum. The binding energy can be calculated as the reaction energy of moving an adsorbed NH_3 to a noninteracting gas-phase environment, formulated by the equation shown in Fig. 2, where E_{ZNH_4}, E_{ZH}, and E_{NH_3} are DFT-computed energies of a zeolitic Brønsted acid with, without NH_3 adsorbate, and isolated gaseous phase NH_3, respectively. Binding energies are typically found to be in the range of 130 kJ mol^{-1}.

2.3 AIMD Potentials of Mean Force

Raw DFT-computed probe molecule binding energies include only the 0-K electronic contributions to binding. While typically good reporters of chemical reactivity, comparisons with experimental observations, such as observed NH_3 temperature programmed desorption profiles, are facilitated by the incorporation of finite temperature effects, including the temperature-dependent entropic and enthalpic contributions to the binding free energy. The most common model to incorporate finite temperature effects is the harmonic oscillator (HO) approximation, appropriate for species that exhibit little conformational flexibility. The HO approximation breaks down when adsorbate motions contain significant anharmonicities or are approximately free translators and/or rotators. Improper treatment of these translational and rotational entropies can lead to underestimation of binding free energies and thus of adsorbate coverages and desorption temperatures (Campbell and Sellers 2012; Paolucci et al. 2014). One approach for incorporating these finite temperature, dynamical effects within a supercell model is AIMD coupled with the potential of mean force (PMF) algorithm, a MD-based umbrella sampling method (Wong and York 2012; den Otter 2013). In the PMF simulation, a relevant reaction coordinate is first defined. For adsorbate binding, the reaction coordinate is most naturally the interatomic distance between adsorbate and adsorbent. MD simulations are performed along the one-dimensional grid of the defined reaction coordinate. For any points on the grid that are away from the equilibrium state, constraint forces are present along the reaction coordinate. The Helmholtz free energy to desorb to the center of the cage is determined by integrating the ensemble-averaged constraint forces along the reaction coordinate from the equilibrium to the desorbed state (Li et al. 2018):

$$\Delta A(T) = -\int_{r_{\mathrm{eq}}}^{r_{\mathrm{max}}} \langle F(r,T) \rangle \, \mathrm{d}r \tag{2}$$

Taking NH_3 binding to a Brønsted acid site in CHA zeolite again as an example (Li et al. 2017), a reaction coordinate was defined as the interatomic separation between the proton and the NH_3 nitrogen center ($d_{\mathrm{H-N}}$), as shown in Fig. 3. Grid points are selected to be sufficiently close to ensure a smooth integration of Eq. (2.3) and sufficiently far to keep computational expense manageable. Twenty discrete values of $d_{\mathrm{H-N}}$ were chosen in the range from 0.9 to 4.5 Å. At each distance, 40 ps of AIMD were performed at 473 K using the CPMD code, and the constraint forces averaged over the second half of trajectories. As the AIMD simulations are rather computational demanding but the simulation quality greatly depends on the sampling time, to estimate the statistical errors, multiple replicate simulations with different initial atomic coordinates were performed at each $d_{\mathrm{H-N}}$. The free energy surface (FES) at 473 K was constructed through integration of constraint forces along $d_{\mathrm{H-N}}$. As suggested by the location of the minimum in the FES, the equilibrium $d_{\mathrm{H-N}} \approx 1.0$ Å, and at distances less than or greater than this separation,

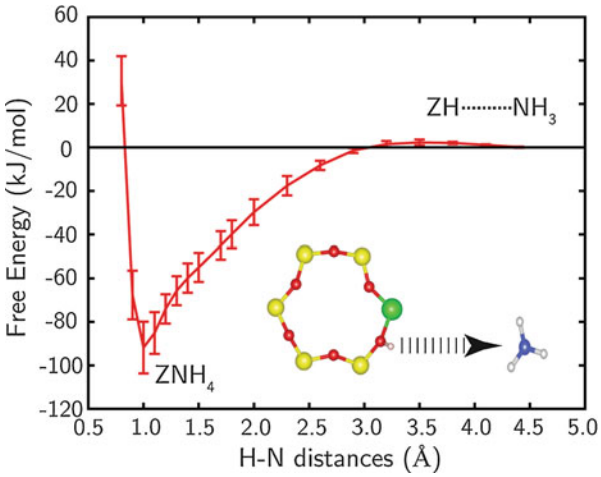

Fig. 3 Free energy profiles for chemisorption of NH_3 to a Brønsted acid site in CHA from PMF simulations (error bars included). Color scheme: O, red; H, pink; Si, yellow; N, blue; Al, green (Li et al. 2017)

the constraint forces are repulsive or attractive, respectively. The FES plateaus as d_{H-N} approaches 4.5 Å, suggesting the NH_3 becomes noninteracting with the Brønsted acid at this separation. To assure that the probe is not perturbed by the framework, the rotational and vibrational dynamics at the end of the constraint path can be compared with those of the free gas. The NH_3 binding free energy at the simulated temperature is the difference between the minimum value and the flat region value in the FES plus the free energy associated with moving the adsorbate from the cage center to outside the zeolite, which is readily estimated (Li et al. 2018).

2.4 Metadynamics Simulations of Brønsted Acid Reactions

The strengths of a Brønsted acid and its local framework environment are both potential factors governing their influence on the rate of an acid-catalyzed reaction. To explore relationship between the nature of a Brønsted acid site and its catalytic function, the intermediates(s) and transition state(s) along the path need to be explicitly identified. The nudged elastic band (NEB) algorithm (Jónsson et al. 1998) and the further refined climbing image NEB (Henkelman et al. 2000) are the most common tools used to locate transition states and minimum energy paths for reactions within the supercell model. As with the geometry optimizations discussed above, these static NEB methods report on the 0-K electronic energy of a particular reaction path and when combined with the harmonic approximation can be used to extract harmonic transition state theory rate constants for use in further microkinetic modeling. However, these static methods are less satisfactory for reactions that

have loosely bound, anharmonic reactant, transition, or product states. A PMF approach is an appropriate alternative when a single reaction coordinate can be clearly identified, but for more complex concerted reactions, the more flexible metadynamics approach is more suitable (Iannuzzi et al. 2003; Laio et al. 2005).

The underlying principle of metadynamics is to supplement the intrinsic DFT potential energy surfaces with a series of Gaussian-shaped biasing potentials accumulated during the course of the AIMD trajectory. These biasing potentials, if introduced as small perturbations through the course of a dynamics trajectory, can smoothly drive the system away from one equilibrium state toward some other region of configuration space of interest. These biasing potentials are applied along predefined collective variables (CV) that can be as simple as a single distance or as complex as a linear combination of many internal degrees of freedom, contributing to the overall flexibility of the method. As with a PMF, metadynamics accelerates the sampling of higher free energy parts of the PES and in particular accelerates the crossing of energy barriers. The collection of biasing potentials accumulated over the course of the simulation reports on the underlying free energy surface, including both the enthalpic and entropic parts of the reaction. The FES of the reaction can be recovered by summing up the biasing potentials added in the defined grid of CV space. To ensure that a particular metadynamics simulation proceeds along a productive direction and to enhance simulation efficiency, CVs should be chosen that are directly relevant to the bond breaking and formation events associated with the reactants and products. Several applications of metadynamics for constructing FES within a supercell model have been reported (Brüssel et al. 2011; Moors et al. 2013; Erichsen et al. 2015).

Here we use the reaction between a Brønsted acid site and two nitrogen oxides (NO_x), a reaction relevant to the Brønsted-acid-catalyzed fast selective catalytic reduction (SCR) of NO_x with NH_3, to illustrate a practical application of metadynamics for a catalytic process (Li et al. 2017). The reactants and products are shown in Fig. 4b. The desired reaction coordinate involves proton (H^+) transfer from a framework oxygen (O_f) to one oxygen of an approaching NO_2 molecule (O_{NO_2}) and concerted adsorption of a NO molecule to an O_f through its N center (N_{NO}). One complication in modeling such a process is that NO at the product stage can potentially coordinate with any one of O_f adjacent to Al and, to obtain a smooth FES and avoid bias, must be included on an equal footing into the CVs. For this purpose one can define a generalized coordination number:

$$\sum_{j\neq i}^{n_{\text{list}}} \frac{1-\left(\frac{d_{ij}}{d_0}\right)^p}{1-\left(\frac{d_{ij}}{d_0}\right)^q}, \tag{3}$$

Here d_{ij} is the distance between atoms i and j, and d_0 is a reference distance corresponding to the approximate bond distance between atoms, and p and q are parameters that determine the balance between sampling bound and unbound regions of the FES. In the simulation illustrated in Fig. 4a, CV1 was set to the

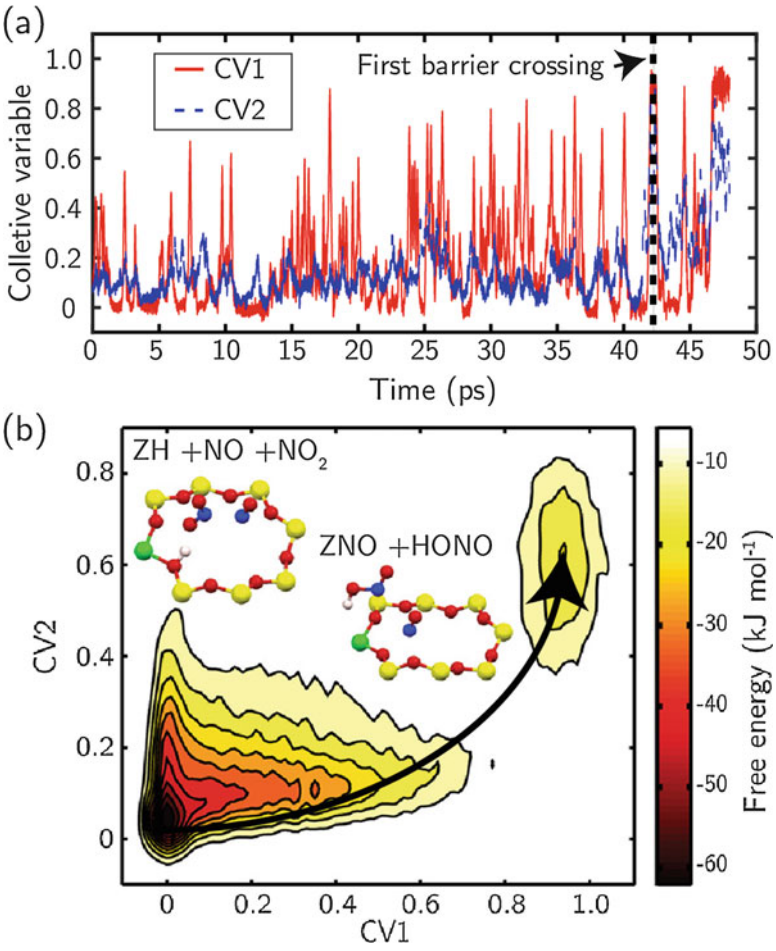

Fig. 4 (**a**) Time evolution of CVs in single run of metadynamics simulation for reaction between NO_x and a Brønsted acid site in CHA at 473 K. (**b**) Free energy surface projected on the two auxiliary collective variables (CV1 and CV2) from metadynamics simulation. Structures of reactants and products are superimposed. Color scheme: O, red; H, pink; Si, yellow; N, blue; Al, green (Li et al. 2017)

$H-O_{NO2}$ CN and CV2 to the O_f-N_{NO} CN, averaged over all four O_f. CV trajectories during the course of the metadynamics simulation are plotted in Fig. 4a. Near the beginning of the simulation, both CVs fluctuate around 0.1, corresponding to a region of configuration space in which $H\text{-}O_{NO_2}$ and $O_f\text{-}N_{NO}$ are unbound and a system in the ZH, NO, NO_2 reactant well. As time progresses, the metadynamics biasing algorithm pushes the system to explore regions of higher CV space. Near 42 ps, both CV1 and CV2 attain values associated with the product state, suggestive of a first crossing of the reaction barrier and formation of ZNO and nitrous acid

HONO. The simulation can be terminated at this point if the purpose is solely to quantify the activation free energy, which corresponds to the depth of the reactant basin in the constructed FES. If the goal is to simulate the full FES including reactant and product basins, simulations are continued until the CV values return to the reactant region so that product free energy basin is well sampled and filled, as shown in Fig. 4b. Metadynamics can in principle be applied to any reactions of interest and is particularly powerful for those reactions with only limited knowledge on the reaction pathways, because CVs are generally loosely defined and the system still retains a high degree of freedom that allows the reaction to proceed through the most favorable pathway on the fly. On the other hand, really free energies depend on careful selection of the parameters that control the rate of addition and size of the biasing potentials.

2.5 Interaction Between Brønsted Sites

We have discussed to this point the properties of an isolated Brønsted site within a zeolite, taking CHA as an example. In real zeolite materials, Al T-sites are generally not ordered, and the silicon to aluminum ratio (SAR) is typically such that there is always some probability for two Al-containing T-sites to be in sufficient proximity to influence chemistry (Paolucci et al. 2017). The distribution of Al within a zeolite framework can in principle be dependent on the types of symmetry-distinct T-sites as well as any interactions between the sites that prevail at the time of synthesis. "Löwenstein's rule," for instance, is the empirical observation that two Al are generally not found in adjacent T-sites. This observation suggests that there may be some energetic interaction between T-sites. This idea has been explored in supercell simulations of paired Brønsted sites in CHA zeolite (Fletcher et al. 2017).

The size of the zeolite supercell determines the maximum unique Al−Al pair combinations that can be represented. Figure 5 shows a representative 36-T-site supercell for CHA. This supercell nominally contains 35 distinct Al−Al pair combinations and, considering that each T-site has 4 distinct associated framework O, 560 Brønsted acid pair configurations. Because of PBC considerations, the actual number of unique combinations is reduced. Figure 5 shows DFT-computed energies for all possible combinations within the 36-T-site supercell. Results are plotted against Al−Al separation and normalized to the energy at infinite Al separation:

$$2\,HSi_{35}AlO_{72} \longrightarrow H_2Si_{34}Al_2O_{72} + Si_{36}O_{72} \tag{4}$$

The broad distribution of energies at any separation reflects the strong dependence of relative energy on proton location. At any given separation, energies span the infinite separation baseline. Further, this range broadens with decreasing Al−Al separation. Energy is minimized at the first-nearest-neighbor separation, suggesting that an Al−O−Al configuration is particularly low in energy when protons are the charge-compensating species and thus that this energy landscape cannot account for Löwenstein's rule. Further, the results suggest that Brønsted acid strength

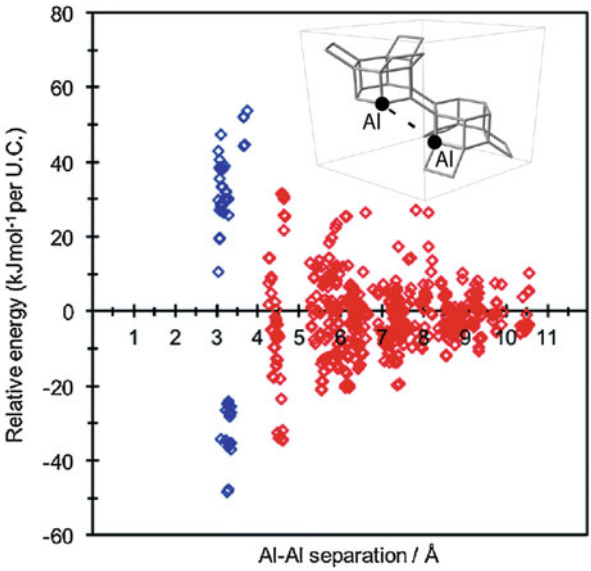

Fig. 5 Relative energy of Brønsted acid site pair against framework aluminum separation for H-SSZ-13 (Fletcher et al. 2017)

is sensitive to the proximity of an acid site to a neighbor. In general, these findings highlight the importance of considering the influence of heterogenous site distributions in zeolite material simulation.

3 Cationic Metal Site Modeling

3.1 Metal Cations Anchored to Isolated Al T-Sites

Metals that can exist as monovalent cations, e.g., alkali metals and some transition metals, are similar to protons in their ability to charge-compensate isolated Al T-sites in zeolites. The same methodologies discussed above can be applied to study the electronic and chemical properties of these cationic metal sites, which are typically Lewis acidic (Thang et al. 2014). For metals that exhibit more than one oxidation state, redox characteristics become relevant. For instance, Cu exists in both 1+ and 2+ oxidation states and thus can in principle charge-compensate one or two Al within a zeolite. Even in the 2+ state, the presence of additional charge-compensating ligands (OH^-) will alter the net charge of the Cu complex and thus its interaction with a zeolite host. Redox cycling between oxidation states has been demonstrated to be key to the performance of Cu-exchanged SSZ-13 zeolites in the standard SCR of NO_x by ammonia (Paolucci et al. 2014, 2017; Gunter et al. 2015). Thus, first-principles models of metal exchange in zeolites become significantly more rich and challenging than that of monovalent Brønsted sites.

3.2 Polyvalent Metal Cations Anchored to Paired Al T-Sites

Because of its relevance to SCR, Cu exchange in CHA zeolites has received considerable computational attention. Figure 6 shows a representation of the CHA cage structure, illustrating the various rings and voids within the zeolite that can host a metal ion (Paolucci et al. 2016b). All T-sites within this structure are equivalent. DFT calculations report that an isolated Cu^{I} ion charge-compensating a single Al T-site seeks a twofold coordinate site, near one O_f adjacent to Al and one one-site removed. Two Al are required to charge-compensate a ligand-free Cu^{II}, and the structure and stability thus becomes a function of the proximity of the two Al. Figure 7 reports DFT-supercell-computed structures of a nominally Cu^{II} ion in a variety of Al pair sites present in CHA, including a second-nearest-neighbor (2NN) Al pair in a four-membered ring (4MR), third-nearest-neighbor (3NN) pairs in six (6MR)- and eight-membered rings (8MR), and fourth-nearest-neighbor (4NN) pairs in an 8MR (Verma et al. 2014). All structures were optimized within a 12-T-site rhombohedral CHA supercell and some repeated in a doubled, 24-T-site supercell to test the sensitivity of computed energies on supercell size. Bader charge analysis on Cu confirms that all Cu are in the same (formally 2+) oxidation state. The structural preference for Cu^{II} for higher coordination is evident in the computed structures, particularly in structure (b).

Computed DFT energies are summarized in Table 1. Relative energies span approximately 1.5 eV and are generally insensitive to supercell size, and among the six configurations explored, configuration (b), corresponding to a Cu^{II} in the 6MR, is substantially lower in energy than other combinations. This energy preference likely reflects the ability of the 6MR to comfortably accommodate the fourfold coordination preference and preferred $Cu^{II}-O$ distances with minimal lattice strain. These energies convolute the energy of interaction of the Cu^{II} ion with the zeolite framework and the energy difference between different Al−Al

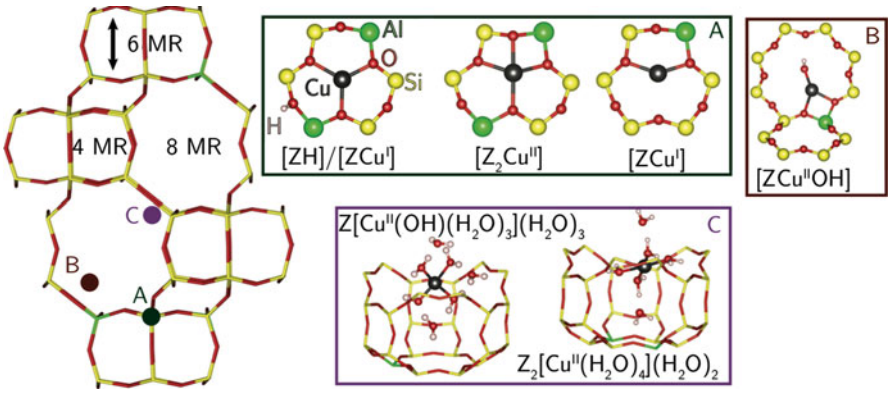

Fig. 6 Side view of the CHA cage structure and computed structures of Cu^{I} and Cu^{II} ions attached to the zeolite framework and solvated by H_2O (Paolucci et al. 2016b)

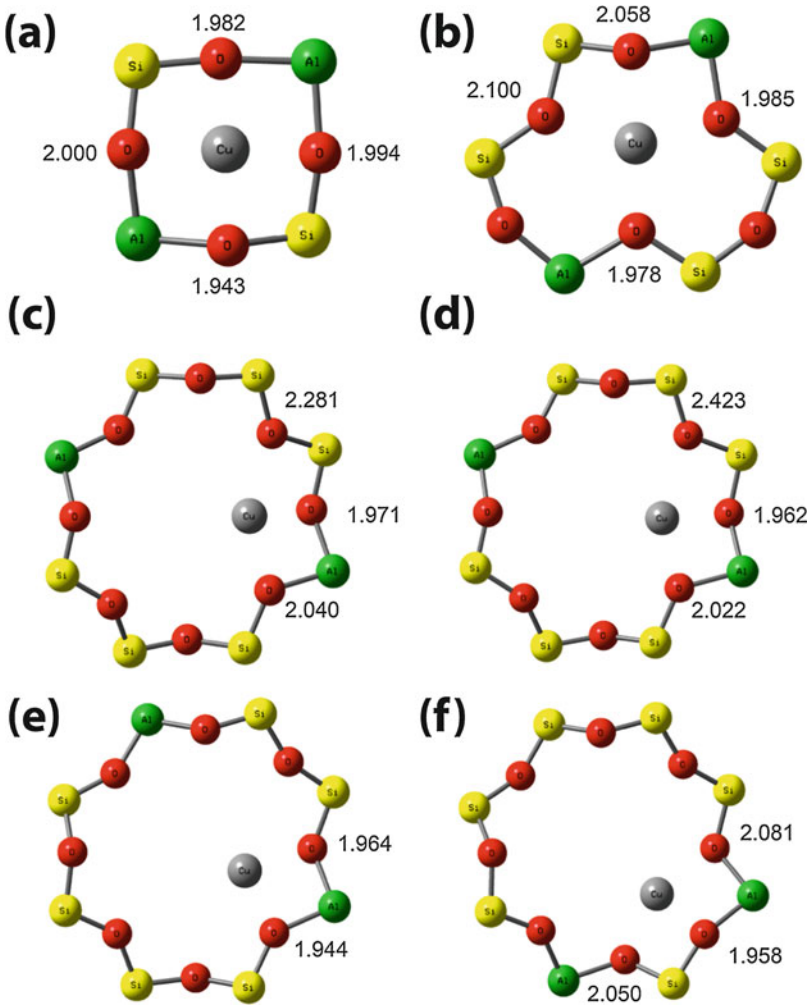

Fig. 7 Relaxed structures of an isolated exchanged Cu^{II} ion in CHA (Verma et al. 2014). Distances between O_f and Cu indicated in Å. (**a**) 2 × 1 × 1 supercell 2NN Al pair in 4MR. (**b**) 2 × 1 × 1 supercell 3NN Al pair in 6MR. (**c**) 2 × 1 × 1 supercell 4NN Al pair in 8MR. (**d**) 1 × 1 × 1 supercell 4NN Al pair in 8MR. (**e**) 1 × 1 × 1 supercell 3NN Al pair in 8MR. (**f**) 1 × 1× 1 supercell 2NN Al pair in 8MR. Color scheme: O, red; Si, yellow; Cu, gray; Al, green

pair combinations. These two factors are not directly separable, and one can only make comparisons on the basis of some balanced reaction involving other charge-compensating species. One can define, for instance, an exchange energy between different sites as

$$Z_2H_{2\,\mathrm{config1}} + Z_2Cu_{\mathrm{config2}} \longrightarrow Z_2H_{2\,\mathrm{config2}} + Z_2Cu_{\mathrm{config1}} \tag{5}$$

Table 1 Raw and relative energies of isolated Cu^{II} ions at different Al pair locations in CHA. All energies in eV (Verma et al. 2014)

Al-pair sites	From 2 × 1 × 1 supercell		From 1 × 1 × 1 supercell	
	Raw energy	Relative energy	Raw energy	Relative energy
2NN in 4MR	−574.622	−0.37	−284.155	−0.37
3NN in 6MR	−575.751	−1.51	−285.203	−1.42
4NN in 8MR	−574.246	0	−283.783	0
3NN in 8MR	N/A	N/A	−283.550	0.23
2NN in 4MR	N/A	N/A	−284.030	−0.25

which convolves the energies shown in Table 1 with those reported in Fig. 5. Exact results depend on site, but it is evident that the 1.5 eV advantage of the 6MR site over others for Cu^{II} overwhelms the $\ll$0.4 eV difference between various Z_2H_2 configurations. Thus, on the basis of this exchange reaction, Cu^{II} will preferentially populate 2Al 6MR sites over other sites, when exchange occurs against the Brønsted form of the zeolite.

3.3 Cu Exchange Siting Between 1Al and 2Al Sites in CHA

As a redox-active ion, Cu^{II} can be present in the zeolite in more than one chemical form. Figure 6 shows the computed structure of ZCuOH, a formally Cu^{II} ion charge-compensated by both a single Al T-site plus an extra-lattice OH^-. DFT calculations show that the addition of this OH^- ligand to an isolated Cu^{I} moves the Cu center from the center of a 6MR up into an adjacent 8MR (Fig. 6), illustrating how Cu location is both a function of the Al site and additional Cu coordination.

In a typical Cu ion exchange experiment, Cu^{II} is introduced to the zeolite as an aqueous solution, Cu is absorbed, and the material is then heated to drive off H_2O. In principle every Al T-site could host a Cu^{II} ion as ZCuOH, leading to a Cu/Al ratio of 1. Ionic Cu uptake in Cu-CHA is typically observed to saturate at Cu/Al ratios lower than unity, however, likely reflecting the competition between 1Al (ZCuOH) and 2Al (Z_2Cu) sites for Cu^{II}. The relative energies of these two types of sites can only be compared by constructing a stoichiometric reaction that connects the two. A variety of choices are possible, but one that is consistent with the conditions of Cu exchange is

$$Z_2Cu^{II}H_2O + ZH \longrightarrow Z_2H_2 + ZCu^{II}OH \tag{6}$$

where H_2O Lewis-bound to Z_2Cu is used to balance the overall reaction and the same Al pair site is implied on both sides of the reaction. The Z_2CuH_2O structure and energy can be evaluated using a computational approach analogous to that described above for NH_3 on a Brønsted site, including AIMD annealing followed

by a relaxation. The H_2O binding energy to a 6MR Z_2Cu evaluated this way is computed to be approximately 0.8 eV (Paolucci et al. 2016b). The overall energy of Eq. (6) can then be computed either in separate single Al and paired Al supercells or in one, larger, supercell that contains both types of sites of interest. Tests indicate that for Cu in CHA, both approaches give similar results and for two Al 3NN in a 6MR give an energy of about 0.6 eV, reflecting an energetic preference for populating these Z_2Cu sites over ZCuOH sites.

Predicting the equilibrium fraction of Z_2Cu and ZCuOH sites in a particular zeolite requires knowledge both of these exchange preferences and the distribution of Al with the framework. This Al distribution is in general a function of the Si to Al ratio (Si/Al) and the zeolite synthesis conditions and cannot be predicted, for instance, from the relative energies of Brønsted sites (Fig. 5). Because CHA contains only a single T-site type, a simple model for the Al distribution is that Al are distributed randomly on the CHA lattice subject to the empirically observed constraint that Al avoid 1NN sites (Löwenstein's rule). This model can be exercised in numerical simulations to predict the distribution of Al as a function of Si/Al. Combining this distribution with a rule derived from Eq. (6) that exchanged Cu^{II} populates 6MR 2Al sites preferentially before populating residual isolated Al sites as ZCuOH leads to the composition phase diagram shown in Fig. 8 (Paolucci et al. 2016b). The white line represents the saturation limit of Z_2Cu sites, and the colored range the relative $ZuOH/Z_2Cu$ fraction. A variety of chemical probes can be used to compare these predictions with observation, including residual Brønsted site density, spectroscopic observation of the ZCuO−H intensity, and chemical titrations using probes sensitive only to paired Al. Paolucci et al. found that these predictions matched experimental observations for Cu-CHA samples of a wide range of Si/Al and Cu/Al ratios prepared under the same conditions.

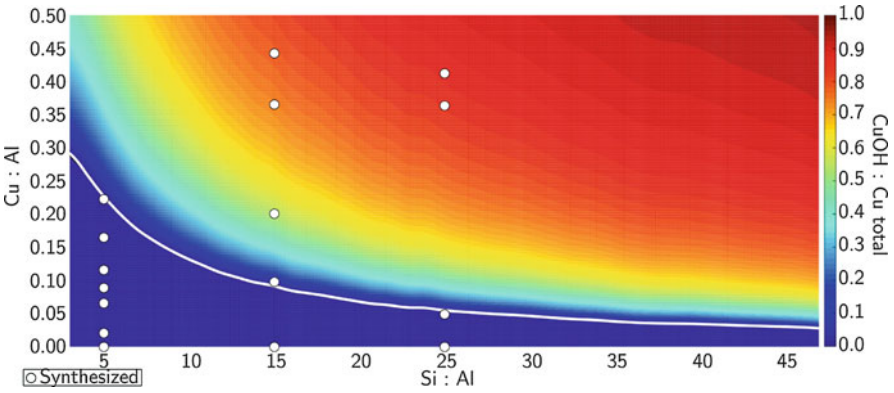

Fig. 8 Predicted Cu site compositional phase diagram versus Si/Al and Cu/Al ratios. Color scale indicates predicted fraction of $ZCu^{II}OH$. White line demarcates transition from Z_2Cu^{II}-only region to mixed $Z_2Cu^{II}/Cu^{II}OH$ region. White circles indicated compositions of synthesized Cu-SSZ-13 samples (Paolucci et al. 2016b)

These results illustrate the potential richness of metal ion exchange in zeolites introduced by polyvalency, extra-lattice ligands, and Al distributions. Cu exchange in CHA is a relatively simple example in which these factors can all be accounted for through DFT evaluation of energies combined with stochastics. These problems become more challenging for lower symmetry zeolites and for metal ions that exhibit more complex exchange chemistry.

3.4 Thermodynamics of Cu Speciation in CHA

Heterogeneous catalytic reactions at metal surfaces are understood in terms of the adsorption, dissociation, rearrangement, and desorption of species at a relatively constant metal (or metal oxide) surface. Metal-exchanged zeolites, while technically heterogeneous catalysts at the macro level, exhibit many of the characteristics of homogeneous catalysts at the atomic scale. As shown in panel C of Fig. 6, isolated Z_2Cu or ZCuOH sites can adsorb multiple ligands (H_2O, in the example shown) and in the process become detached from the zeolite framework itself and move into the void space of the zeolite cage (Kwak et al. 2014; Psofogiannakis et al. 2015; Paolucci et al. 2016b). In the process, Cu centers evolve from a rather static into a dynamic state. Figure 9 compares the volume of space visited during 90 ps of AIMD at 298 K of "dry" and fully hydrated Cu^{II} ions in the CHA cage (Paolucci et al. 2016b); hydration substantially increases this space even at this ambient temperature.

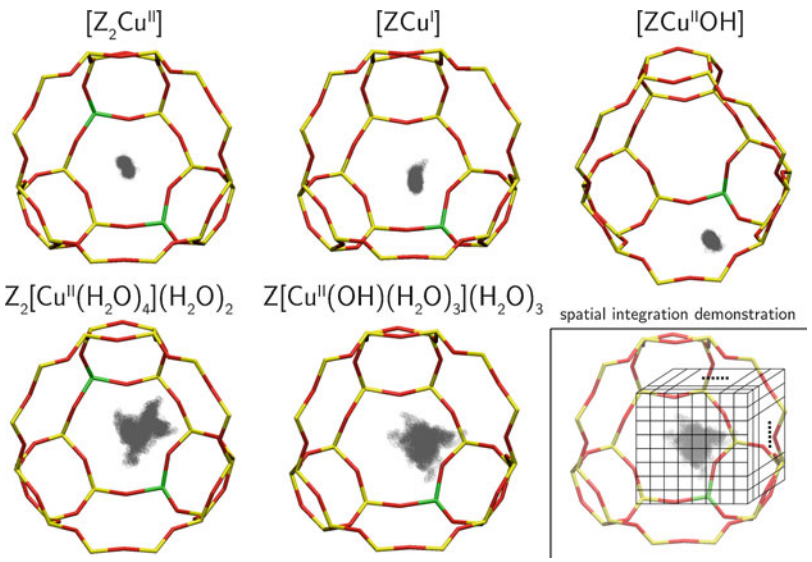

Fig. 9 Volume of space visited by the Cu center during 90 ps of 298 K AIMD as a function of the Cu oxidation and coordination states (Paolucci et al. 2016b)

To compare with and rationalize experimental observations, it is important to be able to predict the equilibrium state of the Cu sites as a function of external conditions, including temperature and pressures of various gases. A first-principles thermodynamic approach is well suited to this problem. In this approach, the various states of a catalyst site are written in terms of formation reactions with respect to some base state of the site and some combination of relevant reactive species. Under hydrothermal conditions, for instance, this formation reaction can be written as

$$\mathrm{Z_*Cu} + \frac{x}{2}\left(\mathrm{H_2O} - \frac{1}{2}\mathrm{O_2}\right) + \frac{y}{2}\mathrm{O_2} \xrightarrow{\Delta G_f} \mathrm{Z_*CuH_xO_y} \tag{7}$$

where $\mathrm{Z_*Cu}$ represents either a single or paired Al site and $\mathrm{H_2O}$ and $\mathrm{O_2}$ are used as reference species for the various ligands that may cover the Cu ion or associate with the lattice itself. Application of this strategy presents two significant challenges: first, to generate a comprehensive list of product species and second, to relate DFT-computed energies to finite temperature free energies. Because the number of candidate species involved is potentially quite large, the AIMD-based free energy approaches of Sects. 2.3 and 2.4 become prohibitively expensive. In such cases, chemical intuition combined with judicious AIMD-based annealings are currently the best alternative. Paolucci et al. used this approach to identify the structures and compute the energies of more than a dozen different candidate combinations of $\mathrm{H_xO_y}$ ligands on both 1Al and 6MR 2Al sites in Cu-CHA (Paolucci et al. 2016b). Further, they used correlations derived from PMF simulations on a limited number of ligands (Paolucci et al. 2014; Li et al. 2018) to estimate the entropic contributions to the free energy. These PMF simulations suggest that adsorbates retain approximately 1/2 of their gas-phase entropy upon adsorption at the highly dynamic Cu sites.

Figure 10 shows the composition phase diagram as a function of $\mathrm{O_2}$ pressure and temperature at a fixed 0.02 bar $\mathrm{H_2O}$ for Cu exchanged near single and paired Al sites. These conditions determine the chemical potentials needed to evaluate the free energy of reaction (7):

$$\Delta G_f^{\mathrm{Z_*CuH_xO_y}}(T, P_{\mathrm{O_2}}, P_{\mathrm{H_2O}}) = \left(E_{\mathrm{DFT}}^{\mathrm{Z_*CuH_xO_y}} - E_{\mathrm{DFT}}^{\mathrm{Z_*Cu}}\right) - T\left(S^{\mathrm{Z_*CuH_xO_y}} - S^{\mathrm{Z_*Cu}}\right) - \frac{x}{2}\mu^{\mathrm{H_2O}}(T, P_{\mathrm{H_2O}}) - \frac{y - x/2}{2}\mu^{\mathrm{O_2}}(T, P_{\mathrm{O_2}}) \tag{8}$$

and the figure reports the composition that minimizes free energy at the specified conditions. These diagrams are a powerful tool for predicting the evolution of sites as a function of conditions. For instance, in Fig. 10, both Cu ions are seen to evolve from a fully hydrated, $\mathrm{Cu^{II}}$ state at ambient conditions (state 1) to a fully dehydrated, zeolite-bound state at elevated temperature (state 2). Thermal "autoreduction" to a $\mathrm{Cu^{I}}$ state is predicted to occur for the ZCuOH sites but not the $\mathrm{Z_2Cu}$ sites. All these observations are in good agreement with experiment, in particular X-ray spectroscopic characterization of oxidation states and coordination numbers

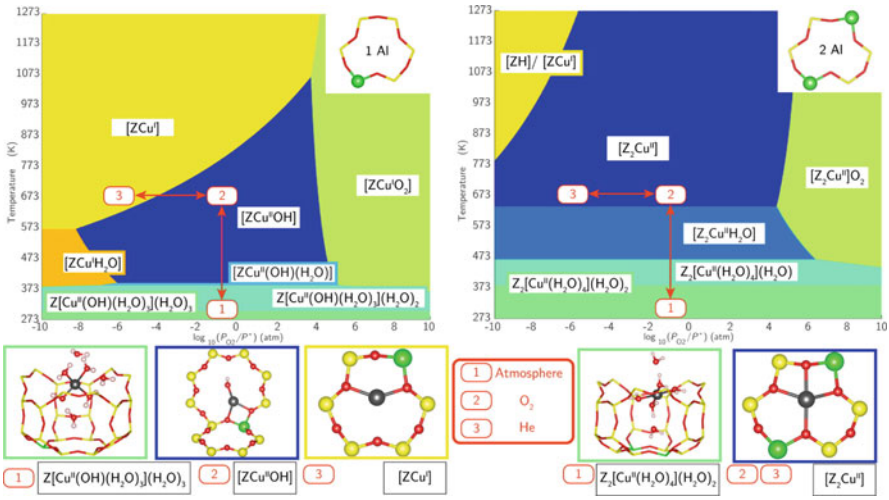

Fig. 10 Ex situ Cu speciation phase diagrams based on HSE06-Tsvdw calculations on 1Al (left) and 2Al (right) Cu exchange sites. Regions indicate site composition that minimizes free energy at 2% H_2O and given T and P_{O_2}. Labeled on the phase diagram and illustrated below are minimum free energy species at (1) ambient (298 K, 20% O_2), (2) oxidizing (673 K, 20% O_2), and (3) inert (673 K, 10^{-6} atm O_2 in He) (Paolucci et al. 2016b)

(Paolucci et al. 2016b). A similar strategy applied to these sites under conditions representative of standard NO_x SCR reveals the role of NH_3 both as a Cu ion ligand and a reductant in this redox chemistry.

4 Outlook and Challenges

The structural and chemical diversity of zeolites presents a rich set of challenges for first-principles computations. We have focused here on the chemistry of Brønsted and Lewis (Cu ion) sites in CHA as two examples for which computational models are well developed and have led to significant insights. The dynamic nature of both types of sites motivates careful consideration of the state of these sites at finite temperature and in the presence of reactive gases. The three-dimensional structure of CHA can be captured in supercells small enough to be amenable to AIMD, but zeolites of lower symmetry and larger supercell volumes remain a challenge for fully first-principles models, as do models able to reliably predict free energy changes upon adsorption and reaction at highly dynamic sites. Zeolite chemistry is closely associated with framework-substituted heteroatoms. While we have focused here on Al, other types of iso- and aliovalent dopants are possible. Further, as we have seen, the distribution of these heteroatoms can itself have an influence on zeolite chemistry by creating local sites and ensembles of differing reactivity, and similar ensemble effects likely are related to zeolite hydrothermal stability as

well. Computational models must account for potential ensemble and environmental effects in any robust comparisons with experiment. For instance, recent experiments demonstrate that ZCuOH but not Z_2Cu sites participate in the selective oxidation of methane to methanol over Cu-CHA (Pappas et al. 2017), a conclusion quite different from that for NO_x SCR (Paolucci et al. 2016b). In fact, recent results highlight the coupled role of Al spatial distributions and adsorbate-induced active site diffusion and pairing in controlling the rate of the O_2-consuming step in standard NO_x SCR (Paolucci et al. 2017). Thus, computational descriptions of zeolite structure and dynamics present a coupled challenge and opportunity for both understanding and predicting heterogeneous catalytic performance.

Acknowledgments This work was prepared in part with the financial support of the BASF Corporation. Numerous valuable discussions with C. Paolucci, H. Li, A. DeBellis, and I. Müller are gratefully acknowledged.

References

Auerbach S, Carrado K, Dutta PK (2003) Handbook of zeolite science and technology. Dekker, New York

Brüssel M, Di Dio PJ, Munñiz K, Kirchner B (2011) Comparison of free energy surfaces calculations from ab initio molecular dynamic simulations at the example of two transition metal catalyzed reactions. Int J Mol Sci 12(2):1389–1409

Campbell CT, Sellers JRV (2012) The entropies of adsorbed molecules. J Am Chem Soc 134(43):18109–18115

Colella C (1996) Ion exchange equilibria in zeolite minerals. Mineral Deposita 31(6):554–562

Corma A (1989) Application of zeolites in fluid catalytic cracking and related processes. In: Jacobs PA, van Santen RA (eds) Zeolites: facts, figures, future part A – Proceedings of the 8th international zeolite conference. Studies in surface science and catalysis, vol 49. Elsevier, Amsterdam pp 49–67. https://doi.org/10.1016/S0167-2991(08)61708-5, http://www.sciencedirect.com/science/article/pii/S0167299108617085

den Otter WK (2013) Revisiting the exact relation between potential of mean force and free-energy profile. J Chem Theory Comput 9(9):3861–3865

Erichsen MW, Wispelaere KD, Hemelsoet K, Moors SL, Deconinck T, Waroquier M, Svelle S, Speybroeck VV, Olsbye U (2015) How zeolitic acid strength and composition alter the reactivity of alkenes and aromatics towards methanol. J Catal 328(Supplement C):186–196

Fletcher RE, Ling S, Slater B (2017) Violations of Lowenstein's rule in zeolites. Chem Sci 8:7483–7491

Gonzales NO, Chakraborty AK, Bell AT (1998) A density functional theory study of the effects of metal cations on the Brønsted acidity of H-ZSM-5. Catal Lett 50(3):135–139

Gunter T, Carvalho HWP, Doronkin DE, Sheppard T, Glatzel P, Atkins AJ, Rudolph J, Jacob CR, Casapu M, Grunwaldt JD (2015) Structural snapshots of the SCR reaction mechanism on Cu-SSZ-13. Chem Commun 51:9227–9230

Hafner J (2008) Ab-initio simulations of materials using VASP: density-functional theory and beyond. J Comput Chem 29(13):2044–2078

Hass KC, Schneider WF, Curioni A, Andreoni W (1998) The chemistry of water on alumina surfaces: reaction dynamics from first principles. Science 282(5387):265–268

Henkelman G, Uberuaga BP, Jónsson H (2000) A climbing image nudged elastic band method for finding saddle points and minimum energy paths. J Chem Phys 113(22):9901–9904

Hernandez-Tamargo CE, Roldan A, de Leeuw NH (2016) A density functional theory study of the structure of pure-silica and aluminium-substituted MFI nanosheets. J Solid State Chem 237:192–203

Iannuzzi M, Laio A, Parrinello M (2003) Efficient exploration of reactive potential energy surfaces using Car-Parrinello molecular dynamics. Phys Rev Lett 90:238302

Jones AJ, Iglesia E (2015) The strength of Brønsted acid sites in microporous aluminosilicates. ACS Catal 5(10):5741–5755

Jónsson H, Mills G, Jacobsen KW (1998) Nudged elastic band method for finding minimum energy paths of transitions. In: Berne BJ, Ciccotti G, Coker DF (eds) Classical and Quantum Dynamics in Condensed Phase Simulations. World Scientific, Singapore, pp 385–404

Kramer GJ, De Man AJM, Van Santen RA (1991) Zeolites versus aluminosilicate clusters: the validity of a local description. J Am Chem Soc 113(17):6435–6441

Kwak JH, Varga T, Peden CH, Gao F, Hanson JC, Szanyi J (2014) Following the movement of Cu ions in a SSZ-13 zeolite during dehydration, reduction and adsorption: a combined in situ TP-XRD, XANES/DRIFTS study. J Catal 314:83–93

Laio A, Rodriguez-Fortea A, Gervasio FL, Ceccarelli M, Parrinello M (2005) Assessing the accuracy of metadynamics. J Phys Chem B 109(14):6714–6721

Li H, Paolucci C, Schneider WF (2018) Zeolite adsorption free energies from ab initio potentials of mean force. J Chem Theory Comput 14(2):929–938. https://doi.org/10.1021/acs.jctc.7b00716

Li S, Zheng Y, Gao F, Szanyi J, Schneider WF (2017) Experimental and computational interrogation of fast SCR mechanism and active sites on H-form SSZ-13. ACS Catal 7(8):5087–5096

Lopez A, Tuilier M, Guth J, Delmotte L, Popa J (1993) Titanium in MFI-Type zeolites: a characterization by XANES, EXAFS, IR, and ^{74,49}Ti and ^{17}O MAS NMR spectroscopy and H_2O adsorption. J Solid State Chem 102(2):480–491

Matsubayashi N, Shimada H, Imamura M, Sato T, Okabe K, Yoshimura Y, Nishijima A (1996) Determination of Fe-substituted sites in the MFI structure by Fe K-edge EXAFS. Catal Today 29(1):273–277

Melson GA, Crawford JE, Crites JW, Mbadcam KJ, Stencel JM, Rao VUS (1983) Evaluation of some new zeolite-supported metal catalysts for synthesis gas conversion, Chap 24. In: Stucky GD, Dwyer FG (eds) Intrazeolite chemistry. American Chemical Society, Washington, pp 397–408

Moors SLC, De Wispelaere K, Van der Mynsbrugge J, Waroquier M, Van Speybroeck V (2013) Molecular dynamics kinetic study on the zeolite-catalyzed benzene methylation in ZSM-5. ACS Catal 3(11):2556–2567

Nicholas CP (2017) Applications of light olefin oligomerization to the production of fuels and chemicals. Appl Catal A Gen 543(March):82–97. https://doi.org/10.1016/j.apcata.2017.06.011

Paolucci C, Verma AA, Bates SA, Kispersky VF, Miller JT, Gounder R, Delgass WN, Ribeiro FH, Schneider WF (2014) Isolation of the copper redox steps in the standard selective catalytic reduction on cu-ssz-13. Angew Chem Int Ed 53(44):11828–11833

Paolucci C, Di Iorio J, Ribeiro F, Gounder R, Schneider WF (2016a) Catalysis science of NO_x selective catalytic reduction with ammonia over Cu-SSZ-13 and Cu-SAPO-34. In: Advances in Catalysis, vol 59. Academic Press, pp 1–107. https://doi.org/10.1016/bs.acat.2016.10.002

Paolucci C, Parekh AA, Khurana I, Di Iorio JR, Li H, Albarracin Caballero JD, Shih AJ, Anggara T, Delgass WN, Miller JT, Ribeiro FH, Gounder R, Schneider WF (2016b) Catalysis in a cage: condition-dependent speciation and dynamics of exchanged cu cations in SSZ-13 zeolites. J Am Chem Soc 138(18):6028–6048

Paolucci C, Khurana I, Parekh AA, Li S, Shih AJ, Li H, Di Iorio JR, Albarracin-Caballero JD, Yezerets A, Miller JT, Delgass WN, Ribeiro FH, Schneider WF, Gounder R (2017) Dynamic multinuclear sites formed by mobilized copper ions in NO_x selective catalytic reduction. Science 357:898–903

Pappas DK, Borfecchia E, Dyballa M, Pankin IA, Lomachenko KA, Martini A, Signorile M, Teketel S, Arstad B, Berlier G, Lamberti C, Bordiga S, Olsbye U, Lillerud KP, Svelle S, Beato P (2017) Methane to methanol: structure-activity relationships for Cu-CHA. J Am Chem Soc 139(42):14961–14975. https://doi.org/10.1021/jacs.7b06472

Psofogiannakis GM, McCleerey JF, Jaramillo E, van Duin ACT (2015) ReaxFF reactive molecular dynamics simulation of the hydration of Cu-SSZ-13 zeolite and the formation of Cu dimers. J Phys Chem C 119(12):6678–6686

Rozanska X, van Santen RA, Demuth T, Hutschka F, Hafner J (2003) A periodic DFT study of isobutene chemisorption in proton-exchanged zeolites: dependence of reactivity on the zeolite framework structure. J Phys Chem B 107(6):1309–1315

Rybicki M, Sauer J (2015) Acidity of two-dimensional zeolites. Phys Chem Chem Phys 17:27873–27882

Sauer J, Hobza P, Zahradnik R (1980) Quantum chemical investigation of interaction sites in zeolites and silica. J Phys Chem 84(24):3318–3326

Schneider W, Hass K, Ramprasad R, Adams J (1998) Density functional theory study of transformations of nitrogen oxides catalyzed by cu-exchanged zeolites. J Phys Chem B 102(19):3692–3705

Sherry HS (1966) The ion-exchange properties of zeolites. I. Univalent ion exchange in synthetic faujasite. J Phys Chem 70(4):1158–1168

Sherwood P, de Vries AH, Collins SJ, Greatbanks SP, Burton NA, Vincent MA, Hillier IH (1997) Computer simulation of zeolite structure and reactivity using embedded cluster methods. Faraday Discuss 106:79–92

Sierka M, Sauer J (2001) Proton mobility in chabazite, faujasite, and ZSM-5 zeolite catalysts. Comparison based on ab initio calculations. J Phys Chem B 105(8):1603–1613

Sierka M, Sauer J (2005) Hybrid quantum mechanics/molecular mechanics methods and their application. Springer, Netherlands, pp 241–258

Thang HV, Rubeš M, Bludský O, Nachtigall P (2014) Computational investigation of the Lewis acidity in three-dimensional and corresponding two-dimensional zeolites: UTL vs IPC-1P. J Phys Chem A 118(35):7526–7534

Trout BL, Chakraborty AK, Bell AT (1996) Local spin density functional theory study of copper ion-exchanged zsm-5. J Phys Chem 100(10):4173–4179

Tuma C, Sauer J (2006) Treating dispersion effects in extended systems by hybrid MP2:DFT calculations-protonation of isobutene in zeolite ferrierite. Phys Chem Chem Phys 8:3955–3965

Verma AA, Bates SA, Anggara T, Paolucci C, Parekh AA, Kamasamudram K, Yezerets A, Miller JT, Delgass WN, Schneider WF, Ribeiro FH (2014) No oxidation: a probe reaction on Cu-SSZ-13. J Catal 312(Supplement C):179–190

Wong KY, York DM (2012) Exact relation between potential of mean force and free-energy profile. J Chem Theory Comput 8(11):3998–4003